Enzyme-based kinetic modelling of ASC–GSH cycle during tomato fruit development reveals the importance of reducing power and ROS availability

Guillaume Decros[1] (iD), Thomas Dussarrat[1] (iD), Pierre Baldet[1] (iD), Cédric Cassan[1,2] (iD), Cécile Cabasson[1,2] (iD), Martine Dieuaide-Noubhani[1] (iD), Alice Destailleur[1], Amélie Flandin[1,2], Sylvain Prigent[1,2] (iD), Kentaro Mori[1] (iD), Sophie Colombié[1,2] (iD), Joana Jorly[1], Yves Gibon[1,2] (iD), Bertrand Beauvoit[1] (iD) and Pierre Pétriacq[1,2] (iD)

[1]INRAE, UMR1332 BFP, University of Bordeaux, Villenave d'Ornon, 33882, France; [2]Bordeaux Metabolome, MetaboHUB, PHENOME-EMPHASIS, Villenave d'Ornon, 33140, France

Authors for correspondence:
Pierre Pétriacq
Email: *pierre.petriacq@inrae.fr*

Guillaume Decros
Email: *decros@mpimp-golm.mpg.de*

Summary

• The ascorbate–glutathione (ASC–GSH) cycle is at the heart of redox metabolism, linking the major redox buffers with central metabolism through the processing of reactive oxygen species (ROS) and pyridine nucleotide metabolism. Tomato fruit development is underpinned by changes in redox buffer contents and their associated enzyme capacities, but interactions between them remain unclear.

• Based on quantitative data obtained for the core redox metabolism, we built an enzyme-based kinetic model to calculate redox metabolite concentrations with their corresponding fluxes and control coefficients.

• Dynamic and associated regulations of the ASC–GSH cycle throughout the whole fruit development were analysed and pointed to a sequential metabolic control of redox fluxes by ASC synthesis, NAD(P)H and ROS availability depending on the developmental phase. Furthermore, we highlighted that monodehydroascorbate reductase and the availability of reducing power were found to be the main regulators of the redox state of ASC and GSH during fruit growth under optimal conditions.

• Our kinetic modelling approach indicated that tomato fruit development displayed growth phase-dependent redox metabolism linked with central metabolism via pyridine nucleotides and H_2O_2 availability, while providing a new tool to the scientific community to investigate redox metabolism in fruits.

Introduction

Reactive oxygen species (ROS) and major redox buffers, namely ascorbate (ASC), glutathione (GSH) and pyridine nucleotides (NAD(H) and NADP(H)) are key partners in orchestrating the redox poise in developing cells (Considine & Foyer, 2021). The ascorbate–glutathione (ASC–GSH) cycle links those redox buffers together in a *ménage-à-trois* allowing rapid ROS processing while controlling the redox state of major antioxidants (Foyer & Noctor, 2011; Decros *et al.*, 2019a). However, measuring ROS is technically challenging due to their high reactivity, which leads to a scarcity of available quantitative data (Queval *et al.*, 2008; Jozefczak *et al.*, 2015; Foyer, 2018). Moreover, redox metabolism has often been specifically quantified during a definite event but not continuously during the development, especially for fruits in which they have been assayed mainly in post-harvest conditions (Liu *et al.*, 2016; Valenzuela *et al.*, 2017). Furthermore, a study in tomato fruit showed that the pyridine nucleotide metabolism is very dynamic during development and pointed to the importance of redox functions (Decros *et al.*, 2019b). Nevertheless, no studies

including all three partners of the ASC–GSH cycle, as well as their redox state and the associated ROS content have yet been reported (Roch *et al.*, 2020).

The dynamic depiction of redox fluxes by deciphering redox signatures in plant biology is exceptionally tedious, if not impossible, probably due to the extreme reactivity of ROS and the intricacy of the redox hub (Mittler *et al.*, 2022). Multiple studies have evaluated the ASC–GSH cycle in photosynthetic cells (Foyer & Noctor, 2016; Foyer, 2018; Hashida *et al.*, 2018; Terai *et al.*, 2020). For decades, targeted studies based on reverse genetics and enzyme purification have focused on the functional and biochemical characterisation of the ROS processing enzymes of the ASC–GSH cycle (Mhamdi *et al.*, 2010; Sofo *et al.*, 2015; Ortiz-Espín *et al.*, 2017). However, metabolic control analysis in plant biology demonstrated that the influence of a specific enzyme could not be solely inferred from its over- or under-expression, and that all enzymes and metabolites in the system needed further consideration (Thomas *et al.*, 1997). Therefore, a promising alternative to measurements of redox pools and antioxidant systems is the use of mathematical modelling of

metabolism (Rohwer, 2012; Salon *et al.*, 2017), as it allows for investigating fluxes and their controlling factors by describing metabolic networks with detailed reactions (Schallau & Junker, 2010). For instance, previous kinetic models of the ASC–GSH cycle have been developed, including studies on the mechanism of ascorbate peroxidase (APX), which demonstrates a great sensitivity of the cycle in response to NADPH photoproduction or consumption by the Calvin-Benson cycle (Valero *et al.*, 2009, 2015). Moreover, the authors indicate that the ASC turnover is mainly independent of GSH metabolism and that NAD(P)H availability indirectly influences the GSH redox state (Tuzet *et al.*, 2019). However, cross-validation of these models using independent datasets remains a critical limitation.

The present study provides the first quantitative and dynamic description of the core redox metabolism during fruit development through an enzyme-based kinetic model of the ASC–GSH cycle. The experimental dataset containing both metabolite concentrations and enzymatic capacities obtained for tomato allowed parameterisation of the model. Computations allow us to calculate steady-state fluxes with concentrations of ROS and major redox buffers and to perform sensitivity analysis. This valuable tool is used to explicit the key controllers of reactive redox metabolism and, more specifically, ascorbate metabolism during fruit development.

Materials and Methods

Plant material and growth conditions

Tomato fruit pericarps were obtained from *Solanum lycopersicum* L. var. M82 under its determined form. Ascorbate-enriched MicroTom plants came from an ethyl methyl sulfonate (EMS) mutant bank that has been previously characterised (Deslous *et al.*, 2021). ASC-enriched EMS mutant plants harbouring the causal mutation responsible for the phenotype were out-crossed with *Solanum lycopersicum* L. var. M82 during six generations (OC6) to obtain plants with the ASC^+ phenotype in the M82 genetic background with a negligible proportion of MicroTom genome ($< 2\%$). Besides CRISPR-Cas9, plants mimicking the causal mutation identified in the EMS line were also generated and out-crossed with *Solanum lycopersicum* L. var. M82 during three generations (OC3) allowing to obtain a M82-like phenotype enriched in ASC. After sowing, OC3F1 and OC6F1 seeds resulted in WT-like (50%) and heterozygous (50%) plants. Both out-crossed lines with original EMS- and CRISPR-lines were cultivated together with the WT M82 plants as well as the WT-like plants from the two out-cross progenies that were defined as control. Each plant line (Mutants, WT M82, WT-like from both EMS and CRISPR crossed lines) and their corresponding fruits were used individually. Remarkably, no difference was observed between the WT M82 and these WT-like in terms of plant growth, fruit growth as well as fruit metabolite content (Supporting Information Fig. S1). Thus, to simplify the results presentation, data from mutant lines have been pooled and compared to, what we consider as the more relevant reference, which is the real WT M82 to build figures.

Tomato plants were grown under usual production glasshouse conditions from February to July, using a long day photoperiod (16 h : 8 h, day : night) and a temperature of 25°C during days and 20°C during nights. Plants were randomised on two tables of 24 plants allowing them to distribute at least nine plants for each genetic condition.

Flower pollination and monitoring of fruit age For control and WT plants, self-pollination was obtained by gentle vibration of the fully opened flower at anthesis. For the ascorbate-enriched plants, which are impaired in pollen fertility and thus in self-pollination, flower emasculation was performed at the anthesis stage. Then, pollen from flowers of WT plants was used and thoroughly applied to the stigma by scraping the inner face of a fully opened cone or by using a brush. To ensure the cross-pollination, this operation was repeated at least three times on the same emasculated flower. The age of the fruit was recorded by tagging flowers on the day of their fertilisation, and the corresponding age was calculated for harvesting.

Fruit sampling Fruits were harvested according to their fertilisation tag. Tomato fruit pericarp was used for the quantitative analysis of metabolite contents and enzyme activities. For anthesis and 4 DPA stages, fruits were entirely frozen as it was too difficult to obtain a separate pericarp quickly enough to avoid stress due to wounding, while for other stages, a 1 cm thick central strip in the fruit pericarp was taken, cut into *c.* 2 mm sections and immediately frozen in liquid nitrogen in scintillation vials to preserve redox metabolites. For each line and each stage, three vials containing at least three fruits from different plants were prepared. All further analyses were conducted using the three biological replicates ($n = 3$).

Targeted metabolic assays

Extraction for redox metabolite assays Extraction of major redox metabolites in both their oxidised and reduced form requires performing two types of extraction adapted from (Queval & Noctor, 2007; Pétriacq *et al.*, 2012; Decros *et al.*, 2019b), which are described in the following sections.

Acidic extraction Extraction of total ASC, total GSH, NAD^+ and $NADP^+$ was performed using 0.1 M HCl and with a ratio of 10 mg of ground fresh weight (FW) for 100 µl. The tubes were then shaken vigorously (vortexed for 1 min) and centrifuged for 10 min at 12 000 ***g*** at 4°C. The supernatant was then split into three: (1) directly used for ASC assay; (2) heated at 95°C for 5 min and used for $NAD(P)^+$ assays; and (3) neutralised for GSH quantification. For the latter, 50 µl of sodium phosphate buffer pH 5.6 and 15 µl of 1 M NaOH were added to 200 µl of supernatant to obtain a final pH 4.5–5. Extracts were kept on ice and in the dark to avoid degradation and utilised within hours to perform the redox analyses.

Basic extraction Extraction of NADH and NADPH was performed using 0.1 M NaOH and with a ratio of 10 mg of ground

FW for 100 µl. The tubes were then shaken vigorously (vortexed for 1 min) and centrifuged for 10 min at 12 000 g at 4°C. The supernatant was then incubated at 95°C for 5 min to allow the degradation of the remaining oxidised forms. Extracts were kept on ice and in the dark to avoid degradation and utilised within hours to perform the redox analyses.

Ascorbate quantification assay The ascorbate assay is based on the capacity of ASC to chemically reduce methylthiazolyldiphenyl-tetrazolium bromide (MTT) to its formazan that absorbs at 570 nm (White & Kennedy, 1985). Besides, the same assay with a supplemental step, 20 µl of 5 mM dithiothreitol (DTT) treatment followed by 10 min incubation at room temperature and then 10 µl of 0.5% NEM was performed to reduce all the ASC present in the extract and thus allow the determination of total ASC content. The difference between total and reduced ascorbate assays allows determining of the ASC oxidised and thus redox state, that is, the ascorbate oxidation ratio.

Glutathione quantification assay The glutathione assay relies on the GR-dependent reduction of 5,5-dithiobis(2-nitro-benzoic acid; DTNB, Ellman's reagent), monitored at 412 nm (Queval & Noctor, 2007). Without pre-treatment of extracts, the method measures total glutathione. The specific measurement of GSSG was achieved by pre-treatment of 200 µl of neutralised extract with 4 µl of 2-vinylpyridine (VPD), resulting in free GSH sequestration. Then, the treated extract was incubated for 30 min at room temperature and sequentially centrifuged two times at 12 000 g for 15 min at 4°C to precipitate VPD. Finally, the treated supernatant was assayed for total glutathione but using a standard curve based on GSSG, ranging from 0 to 50 µM.

Pyridine nucleotides quantification assay Total cellular soluble pools of NAD^+, NADH, $NADP^+$ and NADPH were measured from fruit pericarps of nine developmental stages of tomato fruit according to a coupled enzyme assay adapted from Pétriacq et al. (2012) using either alcohol dehydrogenase (ADH) or glucose-6-phosphate dehydrogenase (G6PDH). Briefly, 5–10 µl of the extract was added to the same volume of neutralisation solution (0.1 M NaOH or 0.1 M HCl for acid or basic extract, respectively), then 20 µl of 0.2 M Tricine/KOH buffer pH 9, 10 mM $MgCl_2$, 4 µl of 200 mM EDTA, 10 µl of 10 mM MTT, 5 µl of 4 mM PES and (2 µl 50% EtOH + 1 µl ADH at 2000 U ml^{-1}) or (2 µl 250 mM G6P + 1 µl 500 U ml^{-1} G6PDH) for NAD(H) or NADP(H), respectively. Optical density was recorded at 570 nm before and after the addition of enzymes for a few minutes. Meanwhile, standard solutions ranging from 0 to 5 µM were added to the microplate for calibration.

H_2O_2 quantification assay The H_2O_2 assay was adapted from a previously described assay in tomato fruits and has been selected for this study due to its non-interference by ASC in tomato (Junglee et al., 2014). Shortly, 10–100 mg, depending on the growth stage, of ground fresh material was directly homogenised with 700 µl of a solution containing 175 µl of TCA (0.1%; w/v), 350 µl of 1 M KI and 175 µl of 10 mM phosphate buffer pH 8 at

4°C for 10 min and protected from light. Meanwhile, a second sample aliquot was treated in the same way by replacing KI with H_2O as a control sample. Next, the homogenate was centrifuged at 12 000 g for 15 min at 4°C and 150 µl of supernatant was transferred in microplate wells and optical density was recorded until stabilisation and compared with a calibration curve of fresh H_2O_2.

Trolox antioxidant capacity assay The Trolox equivalent antioxidant capacity (TEAC) was adapted from Marc et al. (2004) and Scalzo et al. (2005) and was applied to ethanolic extract, thus allowing the detection of the total soluble antioxidant capacity only. Briefly, 10 µl of the ethanolic extract was added to 150 µl of $ABTS^{·+}$ solution and the optical density at 740 nm was recorded until it became stable. The $ABTS^{·+}$ solution was previously prepared by mixing 1 g of ABTS, 6 g of manganese oxide and 250 ml of H_2O, which was protected from light and agitated overnight. Then, the solution was filtered through a 22 µM filter and kept at 4°C up to 6 months. Finally, a standard curve of TROLOX® was prepared in absolute ethanol ranging from 0 to 1 mM.

Targeted enzymatic capacity assays Enzyme activities were assayed using a robotised platform at the HiTMe Facility (Bordeaux Metabolome; http://metabolome.cgfb.u-bordeaux.fr/en). Resulting enzyme capacities were expressed in µ- or n-mol g^{-1} of FW per minute for independent bioreplicates ($n = 3$) and checked for statistical significance by ANOVA for global variation and by binary comparison of Student's t-test or Tuckey test ($P < 0.05$).

Extraction for enzymatic assays Extraction of soluble enzymes was performed using 20–50 mg of ground fresh material, depending on the growth stage, to which c. 20 mg of insoluble PVPP was added to neutralise polyphenols, according to Gibon et al. (2004). The supernatants were then collected, a portion of undiluted extract was retained, and a portion of the supernatants was diluted 2, 4, or 8 times with extraction buffer to assay enzyme activities. For the assay of APX, 10 mM sodium L-ascorbate was added to the extraction buffer.

Capacity of monodehydroascorbate reductase Monodehydroascorbate reductase (MDHAR) activity was measured by direct monitoring of the oxidation of NADH to NAD^+. The assay was coupled to ascorbate using ascorbate oxidase to provide the substrate monodehydroascorbate (Dalton et al., 1986; Pritchard et al., 2000). A control reaction was performed concomitantly in the same conditions but in the absence of ASC. NADH consumption was calculated by monitoring the change in absorbance at 340 nm.

Capacity of dehydroascorbate reductase Dehydroascorbate reductase (DHAR) activity was measured by direct monitoring of the rate of NADPH oxidation by Glutathione reductase (GR) at 340 nm. DHAR catalyses the oxidation of GSH into GSSG, allowing NADPH oxidation by GR.

Concisely, 20 µl of the extract was added to 90 µl of 50 mM Hepes/KOH pH 7.5, 5 mM EDTA, 0.5 mM NAPDH and 1 U ml^{-1} of GR. The reaction was initiated by adding 10 µl of either 1 mM DHA or H_2O in the sample and blank well, respectively. Then, the optical density was recorded at 340 nm for 10 min to calculate NADPH consumption.

Capacity of GR Glutathione reductase activity was measured by direct monitoring of the rate of reduction of oxidised glutathione by NADPH oxidation (Pritchard *et al.*, 2000). A control reaction was concomitantly performed in the same conditions but in the absence of GSSG. Then, optical density at 340 nm was recorded for 5 min to calculate NADPH consumption.

Capacity of APX Ascorbate peroxidase activity was measured by direct measurement of the rate of oxidation of ASC to DHA by H_2O_2. The change in absorbance was monitored at 290 nm using UV-spectrometer, according to Asada (1984). The reaction was started by the addition of 5 µl of 100 mM H_2O_2, and absorbance was recorded at 290 nm for 5 min. ASC content was calculated using an extinction coefficient of ASC at 290 nm ($\varepsilon = 2.8 \, l \, mol^{-1} \, cm^{-1}$).

Capacity of superoxide dismutase Superoxide dismutase (SOD) activity was measured by monitoring the inhibition of MTT oxidation compared to a purified commercial enzyme and was adapted from Peskin and Winterbourn (2017). In addition, catalase was added to the reaction mix to process produced H_2O_2 and thus allow a specific reaction between $O_2^{\cdot-}$ and MTT. A control reaction was concomitantly performed in the same conditions but in the absence of xanthine. Finally, absorbance was recorded at 570 nm and calibrated using a standard curve of purified SOD ranging from 0 to 8 units per well.

Capacity of catalase Catalase activity (CAT) was measured by determining the amount of H_2O_2 remaining after a known incubation period (Summermatter *et al.*, 1995). The remaining H_2O_2 was measured by the oxidation of potassium iodide that results in a yellowish colorimetric signal (340 nm) as described earlier in H_2O_2 assay.

Statistical analyses

Univariate analysis Three independent bioreplicates ($n = 3$) were checked for statistical significance by ANOVA for global variation and by binary comparison of Student's *t*-test or Tuckey test ($P < 0.05$).

Metabolic and enzymatic data were checked for normality and heteroscedasticity by Shapiro and Bartlett tests ($\alpha = 0.05$) using R software (https://www.r-project.org). Then, ANOVA and *post hoc* (Tuckey's tests; $P < 0.05$) were realised using the AGRICOLAE package (de Mendiburu, 2021) on R software or directly on METABOANALYST v.5.0 (https://www.metaboanalyst.ca/).

Multivariate analysis Before multivariate statistical analyses, metabolic data were pre-processed to normally distributed data

by performing median normalisation, cube-root transformation and Pareto scaling of the data intensities as described previously (Belouah *et al.*, 2019). Normalised datasets were then used to construct score plots of Principal Component Analysis (PCA) overview using METABOANALYST v.5.0 (http://www.metaboanalyst.ca/) or via the FACTOEXTRA and FACTOMINER packages (Lê *et al.*, 2008; Kassambara & Mundt, 2020).

Then, hierarchical clustering analysis (HCA) and visualisation through heatmaps were performed by Pearson's correlation with complete or ward clustering linkage using METABOANALYST or via the PHEATMAP and CLUSTER packages in R (Kolde, 2019) using significant features previously determined by ANOVA ($P < 0.05$) presented in Table S1.

Enzyme-based kinetic modelling

Computer modelling The model was built from the mass balance equations of the ASC–GSH cycle. The general form of the differential equations used is:

$$\frac{dC_i}{dt} = \sum_{j=1}^{n} n_{i,j} . v_j . \frac{\text{Vol}_j}{\rho}$$

where C_i is the concentration of the ith species (in µmol g^{-1} FW), $n_{i,j}$ is the stoichiometry of the ith species in the reaction j, Vol$_j$ is the volume fraction of the compartment (in ml$_{\text{compartment}}$ ml$_{\text{tissue}}^{-1}$) where the jth reaction occurs, ρ is the tissue density (in g FW ml$_{\text{tissue}}^{-1}$) and v_j is the rate of the jth reaction (mM min^{-1}) involved in the consumption and production of the ith species. The rate equations associated with the biochemical reactions (Table S2), and the parameters, both time-dependent (measured capacity ($V_{\max}$) of enzymes, volume fraction of compartments...) and constant parameters, are listed in Tables S3, S4, respectively. The set of eight differential equations listed in Table S5 was solved by the COPASY 4.34 software (Hoops *et al.*, 2006) to satisfy the steady-state condition of metabolic intermediates, that is, dC/dt close to zero.

Cytosolic and vacuolar volume fractions were obtained from a previous kinetic-based model focused on vacuolar sugar transport in growing tomato fruit (Beauvoit *et al.*, 2014). The tissue contents of ASC, GSH and H_2O_2 at steady-state were calculated by taking into account the local concentrations of the metabolites given by the model, the compartment volume and the tissue density, according to the following equation:

$$X_{\text{total}} = \frac{[X]_{\text{vac}} . V_{\text{vac}} + [X]_{\text{cyt}} . V_{\text{cyt}} + [X]_{\text{apo}} . V_{\text{apo}}}{\rho}$$

where X_{total} is the tissue content of the metabolite X (in µmol g^{-1} FW) and the subscripts vac, cyt, and apo represent the volume fraction (in ml ml$_{\text{tissue}}^{-1}$) and the steady-state concentrations (in mM) for the cytosol, vacuole and apoplast, respectively, and ρ is the tissue density (in g FW ml^{-1}).

Moreover, enzyme capacities and metabolite concentrations were determined by fitting experimental data using linear or non-linear regressions (Dataset S1; Table S3). Since Michaelis–

Menten constants (K_m) can display considerable discrepancies in the literature or database, we used K_m preferably from studies in tomato or other plants and assumed they remain constant during all the tomato fruit development (Table S4).

Model parameter optimisation and resolution Parameter optimisation was performed using the particle Swarm algorithm (Baker *et al.*, 2010) and by minimising an objective score, that is, the sum of the relative squared residuals weighted, according to the following equation:

$$\text{Obj} = \sum_{i=1}^{n} \left(\frac{X_{i\_\text{cal}} - X_{i\_\text{exp}}}{X_{i\_\text{exp}}} \right)^2$$

where Obj is the objective score, n is the total number of variables, X_{i_cal} is the calculated value and X_{i_exp} is the experimental value of a particular variable X_i (i.e. metabolite content, redox ratio). At each developmental stage, the whole iterative process was repeated using the Curta cluster housed by Mésocentre de Calcul Intensif Aquitain (MCIA) and randomised initial conditions to avoid finding only local minima. The 100 best-scoring parameter sets were kept for statistical analysis, at the end of which the median values (Baker *et al.*, 2010) were used to parameter the model to calculate steady-state fluxes, concentrations and to perform sensitivity analysis.

Metabolic control analysis According to the formalism of MCA (Kacser & Burns, 1973; Heinrich & Rapoport, 1974), flux ($C_{V_j}^{J_i}$) and concentration ($C_{V_j}^{X_i}$) control coefficients by a given enzyme are defined as the scaled partial derivative of the simulated values with respect to the enzyme activity:

$$C_{V_j}^{J_i} = \frac{\partial \log_e J_i}{\partial \log_e V_j}$$

and

$$C_{V_j}^{X_i} = \frac{\partial \log_e X_i}{\partial \log_e V_j}$$

where V_j is the activity of the targeted enzyme j; J_i is a given flux and X_i is a given metabolite concentration.

Coefficients were calculated using the implemented function in COPASY 4.34 and a delta factor of 0.001 for fixed parameters. Then, the control exerted by any enzyme j on the total ascorbate content was calculated as follows:

$$C_{V_j}^{\text{ASC\_total}} = \frac{C_{V_j}^{\text{ASC}}.[\text{ASC}] + C_{V_j}^{\text{DHA}}.[\text{DHA}] + C_{V_j}^{\text{MDHA}}.[\text{MDHA}]}{[\text{ASC}] + [\text{DHA}] + [\text{MDHA}]}$$

In addition, enzyme elasticity coefficients by a given metabolite (e.g. substrate) are defined as the scaled partial derivative of the enzyme activity with respect to the metabolite concentration (Table 2, see later):

$$\varepsilon_{X_j}^{V_i} = \frac{\partial \log_e V_i}{\partial \log_e X_j}$$

Statistics and mathematical regressions Data were cube-root transformed and scaled using Pareto scaling before HCA and heat map visualisation using METABOANALYST (https://www.metaboanalyst.ca/) using Pearson correlation-based distance measure and the ward linkage clustering method (Xia *et al.*, 2009).

Linear and nonlinear regressions of the experimental data were performed using the R shiny interface EASYREG (http://sylvainprigent.fr:3838/easyReg/) using basic and NLSTOOLS R packages.

Right-tailed chi-square test for goodness of fit A chi-square goodness of fit test was performed to evaluate the best model that accommodates the experimental measurements (Rios-Estepa *et al.*, 2010). The chi-square is of the form:

$$\chi^2 = \sum_{i=1}^{n} \sum_{t=1}^{m} \frac{(X_{i,t}\text{cal} - X_{i,t}\text{exp})^2}{X_{i,t}\text{exp}}$$

where $X_{i,t}$cal refers to the tissue content of the metabolite i calculated by the model at the developmental stage t and $X_{i,t}$exp is the corresponding measurements. The chi-square value is then used to calculate a right tail P-value and know the degree of freedom df of the dataset. In this case, df is related to the number of measured variables n and to the number of developmental stages m, such as df $= (n-1) \cdot (m-1)$.

In the context of the modelling approach, a non-significant $P > 0.05$ means that there are no statistically significant differences between measured and simulated values throughout development.

Results

### Quantitative description of ASC–GSH cycle in growing tomato fruit

First, we quantitatively measured H_2O_2 as the main ROS, major redox buffers and ASC–GSH cycle enzymatic capacities during ten developmental stages of tomato fruit from anthesis until red ripening (Figs S2–S4). PCA revealed a distinct separation between the three tomato fruit developmental phases, with the first two components explaining 71.1% of the variation in metabolite contents and enzyme capacities. PC1 (51.1%) separated cell division (i.e. anthesis stage, 4 and 8 DPA) from the other developmental stages, and PC2 (20%) segregated cell division and maturation onset (i.e. 35 DPA and Turning) from cell expansion/ripening (Fig. 1a). Concomitantly, the contribution of variables demonstrated a predominant effect of H_2O_2, CAT, SOD, total antioxidant capacity and GSSG along PC2. PC1 further represented MDHAR, total GSH and GR and reduced ASC (Figs 1b, S5).

Besides, HCA revealed a dynamic redox metabolism during development (Fig. 1c). Clustering the variables revealed four
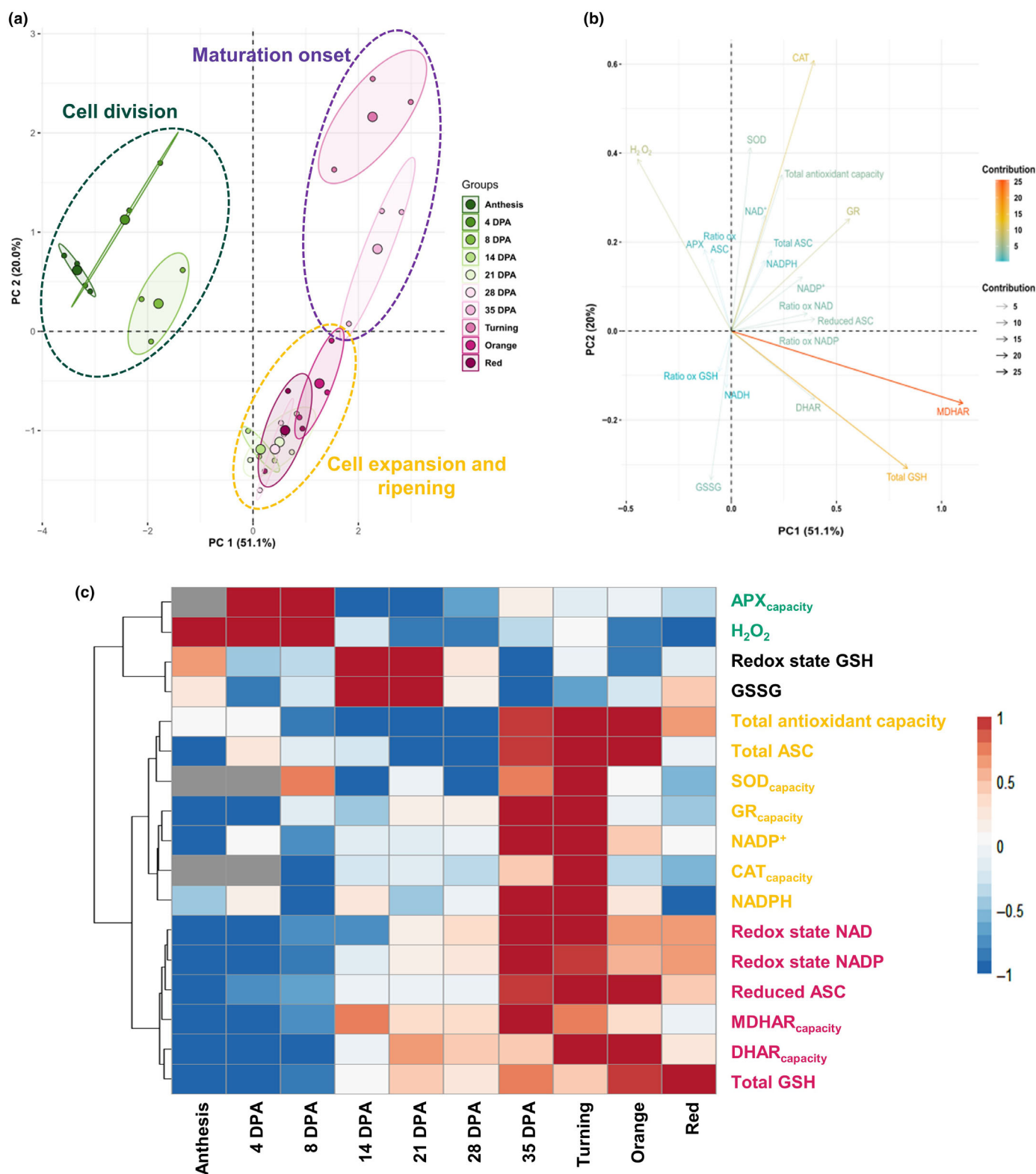
Fig. 1 Core redox metabolism during tomato fruit growth. Normalised metabolites and enzymes capacities of 20 metabolic features of core redox metabolism (see the Materials and Methods section) were visualised (a) for global impact of the growth stage of tomato fruit and (b) features contribution by Principal Component Analysis (PCA with maximal variation given into brackets). The same features were then filtered (ANOVA, $P < 0.05$) and subjected to unidimensional hierarchical clustering analysis (c). Shown are Pearson's correlations after Ward clustering of significant metabolic features. APX, ascorbate peroxidase; ASC, ascorbate; CAT, catalase; DHAR, dehydroascorbate reductase; DPA, days post-anthesis; GR, glutathione reductase; GSH, reduced glutathione; GSSG, oxidised glutathione; H_2O_2, hydrogen peroxide; MDHA, monodehydroascorbate; MDHAR, monodehydroascorbate reductase; $NADP^+$, oxidised nicotinamide adenine dinucleotide phosphate; NADPH, reduced nicotinamide adenine dinucleotide phosphate; SOD, superoxide dismutase.

Fig. 2 Schematic network of ASC–GSH cycle in tomato fruit pericarp cell (a). Dashed arrow stands for non-enzymatic reactions (i.e. chemical reactions and transports), whereas full black arrows stand for enzymatic reactions calculated from metabolic content (v_1–v_5) and blue arrows for optimised fluxes (v_6–v_{12}). Comparison between model predictions and experimental measurements during all fruit development using a model without (b) or with (c) apoplastic H_2O_2 production. Diagonals represent a 100% match between experiments and predictions. Right-tailed chi-square score and corresponding P-values indicate the goodness of model predictions fitting ($\alpha > 0.05$). ABCC, adenosine triphosphate binding cassette subfamily C; apo, apoplast; APX, ascorbate peroxidase; ASC, ascorbate; cyt, cytosol; CAT, catalase; DHA, dehydroascorbate; DHAR, dehydroascorbate reductase; GR, glutathione reductase; GSH, reduced glutathione; GSSG, oxidised glutathione; H_2O_2, hydrogen peroxide; MDHA, monodehydroascorbate; MDHAR, monodehydroascorbate reductase; NAD(P)$^+$, oxidised nicotinamide adenine dinucleotide (phosphate); NAD(P)H, reduced nicotinamide adenine dinucleotide (phosphate); POX, parietal oxidase; ROS, reactive oxygen species; vac, vacuole.
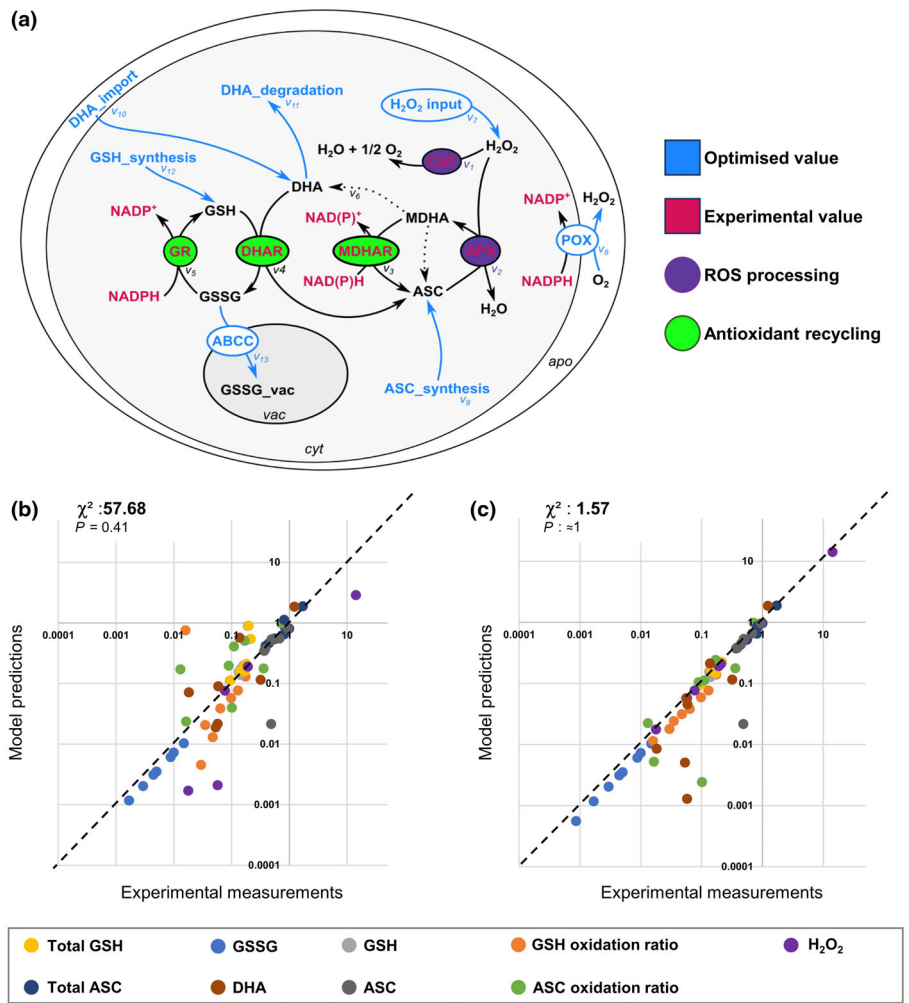
groups, the first (in green) comprising H_2O_2 and APX capacity, which showed their highest values during early fruit development before rapidly dropping and increasing, to a lower extent, during ripening onset. The second and third clusters (in black and yellow, respectively) included variables peaking during phase transitions (beginning of cell expansion and ripening, respectively). Finally, the fourth cluster (in red) included variables that showed their lowest value during cell division and increased continuously throughout fruit development from the cell expansion phase. This cluster contained, in particular, ASC recycling enzyme capacities (DHAR and MDHAR), reduced ASC, total GSH and both oxidation state of NAD and NADP (Figs 1c, S2–S4).

To gain insight into global redox metabolism, we performed untargeted metabolomics to cover a range of secondary antioxidants, including terpenes and phenolics (Methods S1). PCA of the relative intensities of 733 antioxidant features indicated a clear separation between developmental phases (Fig. S6). Overall, our results demonstrate that tomato fruit development is orchestrated by sequential events requiring a dynamic and flexible redox metabolism to handle the strong oxidative metabolism during early stages and to maintain a highly reduced state during the remaining development.

Ascorbate–glutathione model building and initial parametrisation

To calculate redox fluxes, we next constructed a kinetic model of the ASC–GSH cycle that is shared between the cytosol, vacuole and apoplast, where specific reactions occur (Fig. 2a), but we assumed that the enzymatic reactions involved in the model take place in the cytosol. Presumably, it is postulated that the vacuole contains only a few antioxidant metabolites, and its major role is to sequester GSSG, as already reported in a previous modelling study (Tuzet *et al.*, 2019). Thus we assumed that the redox metabolite contents determined using targeted assays are representative of the cytosolic contents. The core network of the model was based on the *Arabidopsis* ASC–GSH cycle described in chloroplasts (Polle, 2001; Valero *et al.*, 2015). However, these previous models focused on plastids and leave tissues and did not take into account either CAT (e.g. mostly peroxisomal; Bernroitner *et al.*, 2009) or MDHAR enzymes. Biochemical reactions, rate equations, parameter setting and corresponding references are listed in Tables S2–S4. The model consisted of eight differential equations based on 18 reactions, 7 of which were enzymatic, and was implemented considering its specific catalytic mechanism (Table S5). A model for each developmental stage from 8 DPA

to Red was generated to be solved at a quasi-stationary state, representing the fruit development as a series of quasi-stationary state models. However, this model suffered from simplifications, including the assumption that NAD(P) concentrations remained constant at each stage, whereas they varied from stage to stage. In addition, the model did not account for the different cellular ROS production sources (photosynthesis, photorespiration and respiration) because the lack of information about their dynamics during fruit growth prevents the parameterisation of such a fine model. Moreover, superoxide synthesis was not implemented in the model, assuming this species to be entirely chemically and enzymatically dismutated to hydrogen peroxide owing to the high catalytic capacity of SOD (Bowler *et al.*, 1994; Valero *et al.*, 2015; Fig. S4f). Additionally, since we did not quantify sub-cellular concentrations of DHA, we made the hypothesis of a global DHA import flux originating from the apoplast, which has been shown to accumulate DHA due to the activity of ascorbate oxidases (AOX) in leaf tissues (Pignocchi & Foyer, 2003; Karpinska *et al.*, 2018). Finally, the model did not include secondary antioxidant metabolites, and we attributed ROS processing to CAT because of its considerable catalytic capacity (Fig. S4b; Tuzet *et al.*, 2019).

Model fitting: The necessity of a spatially controlled ROS production

The initial parameterisation of the model left seven fluxes unknown, namely, H_2O_2 production (v_7), parietal oxidase activity (v_8), ASC synthesis (v_9), DHA import (v_{10}), DHA degradation (v_{11}), GSH synthesis (v_{12}) and GSSG transport in the vacuole (v_{13}; Fig. 2a). We optimised the values of these fluxes or of their parameters (i.e. constant parameters k_x) for each stage by fitting the experimentally measured contents (see the Materials and Methods section). Optimised median parameters were then used to calculate steady-state content in redox buffers, their redox state and total ROS concentration (Baker *et al.*, 2010; Fig. S7).

At first, the optimised median model at 8 DPA showed very low content of reduced ASC and H_2O_2 content while displaying a high ROS production flux (Figs S7, S8). Under these conditions, model predictions concerning H_2O_2 content at 8 and 14 DPA were much lower than the measured content. Without spatial separation between ROS production and enzymatic processing, ROS would be treated immediately either by APX, until it reached its maximum capacity and/or ASC had been totally consumed, or by CAT that could handle supra-physiological ROS production flux. In addition, this parameterisation did not allow the model to reach a steady-state at 35 DPA and thus failed to describe redox metabolism during the whole fruit development. Moreover, the log–log plot showed that this model parameterisation predicted values distant from several experimentally obtained variables (i.e. H_2O_2, GSH, and ASC oxidation ratios and total GSH; Fig. 2b).

To address these limitations, the apoplast was implemented to: account for parietal oxidases as an active ROS-producing system; and allow an extracellular ROS diffusion potentially involved in signalling (Foyer & Noctor, 2016; Decros *et al.*, 2019a). Overall,

values leading to a satisfactory match between predicted and experimental data could be obtained for all unknown parameters and throughout fruit development (Figs 2c, S7). Moreover, the sum of weighted square errors showed a substantial decrease, concomitant with an increase in the right-tailed chi-square *P*-value, thus making the model predictions stronger (Figs 2c, S8–S10). Altogether, our results indicate that the optimised model, including parietal oxidases, allows accurate model predictions during all tomato fruit development.

Model validation using ASC-enriched mutant fruits

To ensure the robustness of model predictions, we performed cross-validation of independent experimental data exploiting a previously characterised mutant line enriched in ASC due to higher ASC synthesis (Deslous *et al.*, 2021). ASC-enriched mutant fruits displayed differences in ASC content without significant discrepancies in either enzymatic capacities of enzymes involved in the ASC–GSH cycle or phenotypical variables allowing us to keep the same parameterisation from the original WT (Figs S11–S14). In the model, an increase in total ASC content was reproduced *in silico* for each developmental stage by enhancing only one parameter: either the input of ASC (v_9) to mimic the rise in synthesis, or the import of DHA (v_{10}) traducing the import from leaf tissues (Fig. 3a). Strikingly, an increase in ASC synthesis led to a sharp accumulation of reduced ASC and thus a swift rise in total ASC content, whereas an increase in DHA input, up to eight times the level of the original model, was not able to induce a significant accumulation of ASC regardless of the developmental stage (Fig. S15). Overall, the *in silico* simulations emphasise that the ASC accumulation observed in mutant fruits can be reproduced by solely enhancing the ASC synthesis of fruit cells.

To analyse the goodness of fit of the mutant data, the WT model was run at each developmental stage by setting the respective ASC synthesis at a value that enabled ASC content to be close to that of the mutant (Table S6). Corresponding predictions regarding redox buffers and ROS were compared, indicating no significant differences with the experimental data at the scale of whole fruit development (Figs 3b, S16). Hence, the two-step modelling approach, that is, parameters optimisation using the WT data only and subsequent cross-validation of the model using independent mutant data, enabled us to investigate the control of major redox buffer content and ROS processing during the whole fruit development.

Dynamics of the ASC–GSH cycle during tomato fruit development

The comparative clustering analysis combining relative growth rate, flux and enzymatic capacity (V_{max}) evolution patterns revealed three distinct clusters (Fig. 4). The first cluster included variables involved in green fruit development before decreasing from 35 DPA until the end of development (e.g. DHAR, GR and GSH synthesis fluxes, MDHAR capacity and fruit relative growth rate). The second cluster encompassed maximal fluxes

Fig. 3 Model cross-validation using ascorbate (ASC)-enriched mutant. Effect of an increase in ASC synthesis (blue) or DHA import (orange) on the pericarp ASC content for three stages (a). Solid lines comprise thousands of model predictions after variations in ASC synthesis or DHA import fluxes compared to the initial wild-type (WT) value. Blue circles represent measured WT values, and red triangles represent the ascorbate-enriched mutant values. Comparison between model predictions and experimental measurements during all fruit development (b) using ASC-enriched mutant data set. The model was run at each developmental stage by setting the respective ASC synthesis at a value that enabled ASC content to be close to that of the mutant. ASC, ascorbate; CAT, catalase; DHA, dehydroascorbate; DPA, day post anthesis; GSH, reduced glutathione; GSSG, oxidised glutathione; H_2O_2, hydrogene peroxide.
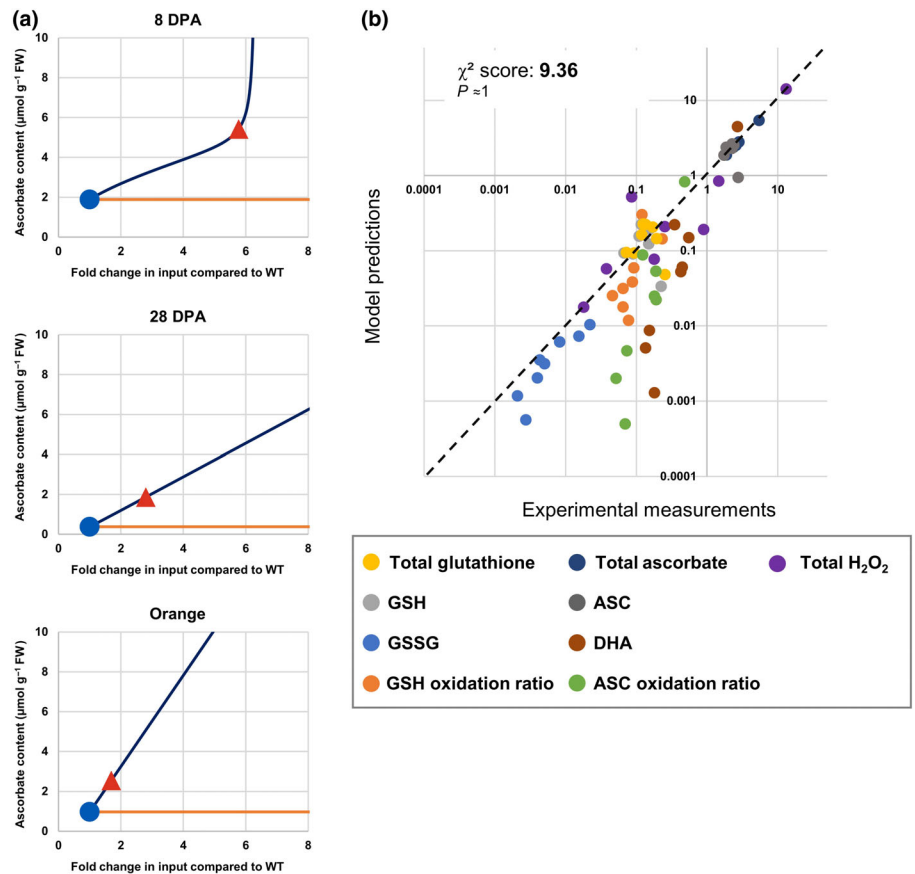
and capacities during cell division before rapidly decreasing during cell expansion, most of which rebounded specifically at the turning stage (e.g. APX, MDHAR, ASC synthesis and chemical recycling of MDHA fluxes). The last cluster separated clearly and contained only V_{max} that were high during fruit division or maturation (Fig. 4). Overall, this HCA indicates that redox metabolism, especially ROS processing and ASC recycling, is mostly represented during fruit cell division and ripening phase.

Next, to understand the regulation of redox fluxes, we performed metabolic control analysis focusing on the fluxes involved in cluster 2 (CAT, APX and MDHAR), which helped determine how much (in %) a given flux would increase or decrease (positively or negatively) if the activity of a given enzyme or metabolic pathway increased by 1%. This allows us to identify three distinct patterns during development. Firstly, for the 8 DPA stage, APX flux was positively controlled mainly by the ASC synthesis and, to a lesser extent, by MDHAR (Fig. S17; Table 1). Concomitantly, CAT flux was only influenced by ROS production, and MDHAR flux was positively controlled by itself (Table 1), thus reflecting a limitation of the MDHAR activity by NAD(P)H supply (Fig. S18; Table 2). Therefore, during fruit cell division, ROS production exceeds the capacity of APX flux, which is limited by the supply of reduced ASC (Fig. S18; Table 2), leading to H_2O_2 accumulation. Hence, during cell division, the activity of the ASC–GSH cycle mainly relies on ROS production, NAD(P)H supply and ASC synthesis (Fig. 5).

Then, at 14 and 21 DPA (i.e. beginning of cell expansion), the APX flux became strongly dependent on MDHAR activity, suggesting that APX still relies on reduced ASC supply and is saturated by ROS (Fig. S17; Table 1). Besides, elasticity coefficients were calculated for APX and MDHAR as described in the Materials and Methods section. These coefficients indicate how much (in %) the enzyme activity would increase if the substrate concentration was increased by 1% (Table 2). Here we showed that MDHAR was still controlled by NAD(P)H supply (Table 2), further indicating that the ASC–GSH cycle was mainly regulated by NAD(P)H content when H_2O_2 provision was high enough to saturate APX. Interestingly, this behaviour was also found during maturation onset with the addition of a strong influence of total H_2O_2 production flux on ASC content and oxidation ratio (Figs 5, S19). At this time, both NAD(P)H content and ROS production flux strongly modulated the ASC oxidation ratio, thus indicating a fine control by central metabolism during the transition from cell expansion to ripening.

Finally, the decrease in ROS production flux at 28 DPA, orange and red stages induced a positive control of APX flux only by the total ROS production (Table 1). Moreover, CAT and APX negatively influence each other, indicating a competition of these enzymes for H_2O_2, which is the limiting substrate. Therefore, the strong decrease in H_2O_2 production resulted in a shift in the behaviour of the ASC–GSH cycle in which the APX
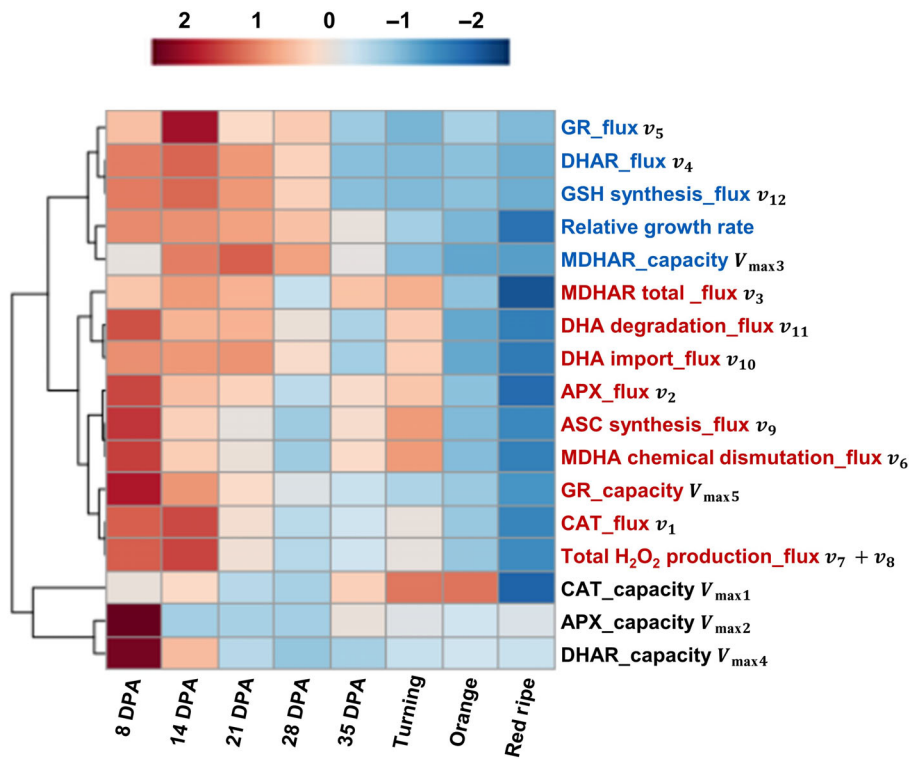
Fig. 4 Unidimensional hierarchical clustering analysis of fluxes and enzymes capacities involved in the ASC–GSH cycle and ROS processing. Normalised flux and enzymes capacities involved in the model were filtered (ANOVA, $P < 0.05$) and subjected to unidimensional hierarchical clustering analysis. Shown are Pearson's correlations after Ward clustering of significant metabolic features. V_{max} and v symbols refer to capacities and fluxes included in the model and represented in Fig. 2. APX, ascorbate peroxidase; ASC, ascorbate; CAT, catalase; DHA, dehydroascorbate; DHAR, dehydroascorbate reductase; DPA, days post-anthesis; GSH, reduced glutathione; GR, glutathione reductase; H_2O_2, hydrogen peroxide; MDHA, monodehydroascorbate; MDHAR, monodehydroascorbate reductase.

Table 1 Metabolic control analysis of APX, MDHAR and CAT fluxes to some enzyme activities.

Flux control coefficient	Growth stage							
	8 DPA	14 DPA	21 DPA	28 DPA	35 DPA	Turning	Orange	Red
APX flux								
$C^{APX}_{Total\ H_2O_2\ production}$	2.20E-08	2.40E-04	0.033	0.67	0.05	0.002	0.876	0.976
C^{APX}_{APX}	5.60E-06	0.032	0.133	0.754	0.057	0.003	0.697	0.437
C^{APX}_{MDHAR}	0.253	0.953	0.859	0.067	0.919	0.886	0.011	0.001
$C^{APX}_{ASC\ synthesis}$	0.75	0.139	0.166	0.04	0.115	0.144	0.006	0.001
C^{APX}_{CAT}	−2.20E-08	−2.40E-04	−0.028	−0.491	−0.034	−0.001	−0.585	−0.413
Total MDHAR flux								
$C^{MDHAR}_{Total\ H_2O_2\ production}$	3.10E-10	2.20E-04	0.032	0.669	0.047	4.60E-04	0.876	0.976
C^{MDHAR}_{APX}	7.80E-08	0.029	0.131	0.753	0.053	0.001	0.697	0.437
C^{MDHAR}_{MDHAR}	1	0.971	0.865	0.068	0.933	0.999	0.012	0.001
$C^{MDHAR}_{ASC\ synthesis}$	0.01	0.126	0.163	0.04	0.107	0.037	0.006	0.001
C^{MDHAR}_{CAT}	−3.00E-10	−2.20E-04	−0.028	−0.491	−0.032	−3.60E-04	−0.584	−0.413
CAT flux								
$C^{CAT}_{Total\ H_2O_2\ production}$	1.025	1.006	1.165	1.12	1.437	1.276	1.062	1.033
C^{CAT}_{APX}	−1.40E-07	−1.90E-04	−0.023	−0.274	−0.026	−0.001	−0.348	−0.594
C^{CAT}_{MDHAR}	−0.006	−0.005	−0.147	−0.024	−0.423	−0.245	−0.005	−0.001
$C^{CAT}_{ASC\ synthesis}$	−0.019	−0.001	−0.028	−0.015	−0.053	−0.04	−0.003	−0.002
C^{CAT}_{CAT}	5.50E-10	1.40E-06	0.005	0.179	0.016	3.90E-04	0.292	0.562

APX, ascorbate peroxidase; ASC, ascorbate; CAT, catalase; DPA, day post anthesis; MDHAR, monodehydroascorbate reductase.
Flux control coefficients were calculated as described in the Materials and Methods section. Such a coefficient indicates how much (in %) a given flux would increase (+ sign) or decrease (− sign) if the activity of a given enzyme or metabolic pathway was increased by 1%. The colours correspond to the fluxes that are most affected, positively in green and negatively in red.

became the controlling step itself, restricted by the H_2O_2 production (Tables 1, 2). Simultaneously, ASC levels and oxidation ratio lost their sensitivity to NAD(P)H content and ROS production (Figs 5, S19), indicating that the ASC–GSH cycle maintains the predominantly reduced ASC pool for stages with very low metabolic activity.

Table 2 Metabolic control analysis of APX and MDHAR enzymes to their substrate concentration.

Elasticity coefficient	Growth stage							
	8 DPA	14 DPA	21 DPA	28 DPA	35 DPA	Turning	Orange	Red
APX activity								
$C^{APX}_{[ASC]}$	0.8	0.082	0.061	0.024	0.02	0.019	0.004	0.002
$C^{APX}_{[H_2O_2]}$	0.004	0.007	0.212	0.652	0.606	0.434	0.838	0.947
NAD-dependent MDHAR activity								
$C^{MDHAR\_NAD}_{[MDHA]}$	0.013	0.158	0.237	0.485	0.078	0.017	0.414	0.799
$C^{MDHAR\_NAD}_{[NADH]}$	0.987	0.837	0.739	0.382	0.918	0.983	0.459	0.113
NADP-dependent MDHAR activity								
$C^{MDHAR\_NADP}_{[MDHA]}$	0.025	0.306	0.429	0.785	0.271	0.085	0.785	0.902
$C^{MDHAR\_NADP}_{[NADPH]}$	0.975	0.677	0.522	0.441	0.726	0.914	0.758	1.074

APX, ascorbate peroxidase; ASC, ascorbate; DPA, day post anthesis; MDHA, monodehydroascorbate; MDHAR, monodehydroascorbate reductase; NAD(P), nicotinamide adenine dinucleotide (phosphate).
Elasticity coefficients were calculated as described in the Materials and Methods section. Such a coefficient indicates how much (in %) the activity of a given enzyme would increase if the concentration of its substrate was increased by 1%. The colours correspond to the fluxes that are most affected, positively in green.
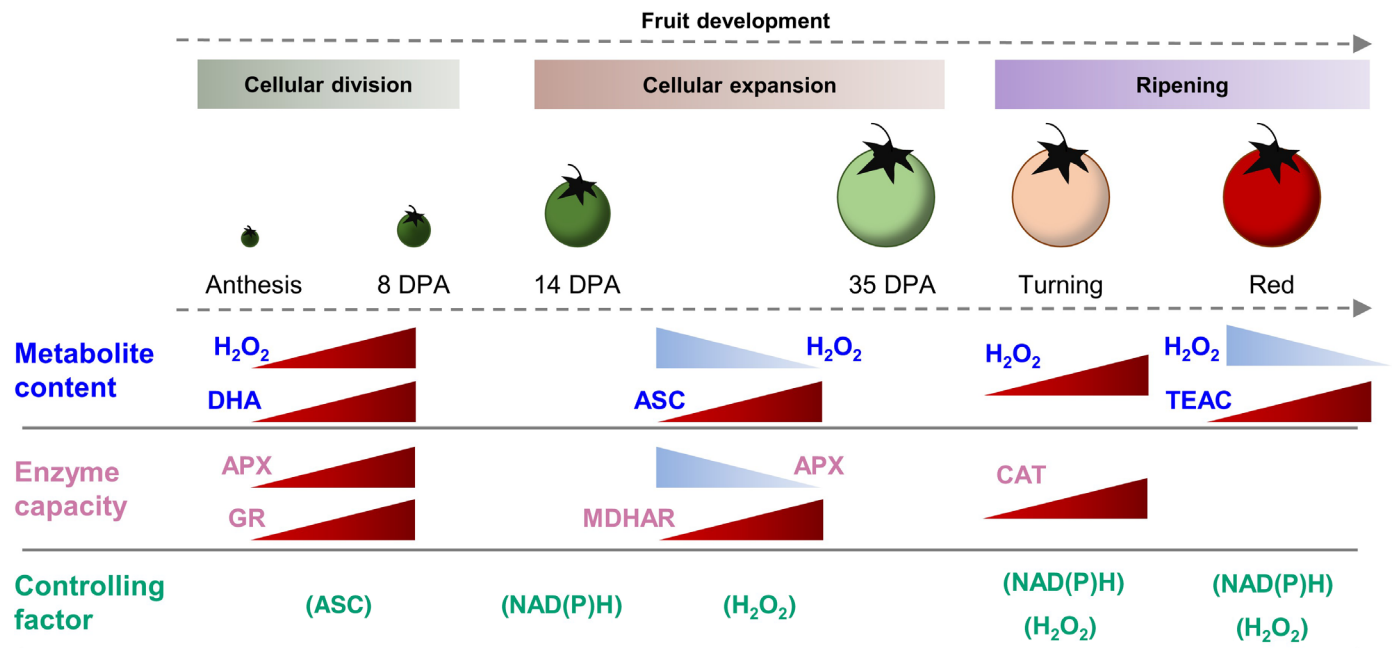
Fig. 5 Major redox changes during fruit development. Each developmental phase of fruit exhibits a specific redox behaviour where the delivery of ASC, NADPH and H_2O_2 appears as the main controlling factor. APX, ascorbate peroxidase; ASC, ascorbate; CAT, catalase; DHA, dehydroascorbate; DPA, days post-anthesis; GR, glutathione reductase; H_2O_2, hydrogen peroxide; MDHAR, monodehydroascorbate reductase; NAD(P)H, reduced nicotinamide adenine dinucleotide (phosphate); TEAC, Trolox equivalent antioxidant capacity.

Discussion

Here, we combined targeted analysis, computational enzyme-based kinetic modelling and global analyses to provide the first dynamic description of core redox metabolism during fruit development. In fruit tissues, redox metabolism has rarely been evaluated in a developmental context, although concepts focusing on APX catalytic mechanism and ASC recycling from circadian clock studies in leaves remain valuable resources (Valero *et al.*, 2009, 2015; Foyer, 2018). From a general perspective, redox metabolism dynamically changed with fruit growth, displaying a sequential activity in a 'wave-shaped' pattern corresponding to the fruit development (i.e. cell division-expansion-ripening) with specific changes at phase transitions (Figs 5, S2–S4). Similarly, central fruit metabolism has also been defined as a 'turbo' metabolism during cell division that rapidly drops at the beginning of cell expansion until growth arrest (Biais *et al.*, 2014; Roch *et al.*, 2020). Moreover, phytohormones have also been reported to fluctuate in a growth-dependent manner during fruit development (Zhang *et al.*, 2009; McAtee *et al.*, 2013).

Uncoupling of ASC and GSH metabolism during early fruit development

The beginning of fruit development revealed an active oxidative metabolism resulting in a remarkably high ROS content despite a strong APX capacity. Simultaneously, ASC recycling enzymes showed low capacities, thus resulting in the nearly complete oxidation of ASC (Figs 1c, S2–S4). Strikingly, such high levels of DHA during young fruit development have been previously reported in diverse fruit species, suggesting a common phenomenon between fruit species (Decros *et al.*, 2019a; Roch *et al.*, 2020). Additionally, fruit development is accompanied by a regulation phenomenon that limits the emergence of hypoxic area (Mori *et al.*, 2019) and no hypoxia response gene expressions in young fruit was not reported in the database (Fernandez-Pozo *et al.*, 2017; Cukrov, 2018). Besides, our models emphasised the necessity of a ROS production source away from the antioxidant system and control of APX by the supply in reduced ASC (Fig. 2c; Table 1). This is in line with previous reports of active fruit photosynthesis during early development and the role of ROS processing by ASC during this process (Pesaresi *et al.*, 2014; Foyer, 2018; Decros *et al.*, 2019b; Quinet *et al.*, 2019). However, tomato fruit also exhibited moderate GSH oxidation, which has been reported to be recruited in the nucleus during early cell proliferation (Markovic *et al.*, 2007; Vivancos *et al.*, 2010). Moreover, DHAR and GR fluxes were separated from total H_2O_2 production, APX and MDHAR fluxes (Fig. 4), indicating that ROS processing in tomato fruit was rather dependent on ASC recycling via MDHAR activity and NAD(P)H consumption. Overall, this strongly suggests that during cell division, ROS accumulate in the same compartment as ASC and APX, resulting in a complete ASC oxidation, without affecting GSH, which remains moderately oxidised and has been reported to be recruited in the nucleus for thiol signalling while lowering the oxidative defence shield during early cell proliferation (Vivancos *et al.*, 2010).

Shift in ASC redox state controlled by MDHAR and reducing power availability during fruit cell expansion

Next, ASC displayed a drastic shift from totally oxidised to fully reduced during the transition from cell division to the expansion phase. Furthermore, it is worth noting that the change in ASC redox state was concurrent with the increase in the fruit growth rate, which emphasises the overall link between growth and redox metabolism (Figs 1c, 4), as already reported in the case of pyridine nucleotides (Decros *et al.*, 2019b). Concomitantly, APX and MDHAR enzyme capacities showed a similar trend from ascorbate oxidation to full recycling (Figs 5, S4). Complementarily, the kinetic model unveiled a simultaneous shift in the ASC–GSH flux sensitivity, starting from a limitation by ASC supply during cell division to a restriction by NAD(P)H availability (Tables 1, 2). Overall, during cell expansion, APX is saturated by H_2O_2, while its supply in reduced ASC was controlled by the MDHAR activity and NAD(P)H provision. Reducing power will have the most substantial impact on the ASC oxidation ratio and, thus, on potential redox signalling (Fig. S19). Moreover, endoreduplication is also a

hallmark of this growth phase transition in which redox metabolism involvement remains an incomplete puzzle (Chevalier *et al.*, 2011; Fanwoua *et al.*, 2013). In addition, ASC has been reported to be present in the nucleus, where it acts as a signalling molecule (Zechmann, 2011). Here, the shift in ASC redox state observed during this phase transition, concurrent with the increase in its recycling capacity through MDHAR, suggests that ASC metabolism participates in the control of the trade-off between division and endoreduplication. Besides, GR and DHAR capacities evolved independently from other redox features, and the model highlighted the uncorrelation between the capacities and fluxes of these enzymes (Fig. 4), which has also been reported for central sugar metabolism (Beauvoit *et al.*, 2014). Similarly, DHAR triple mutants displayed no phenotype or disturbance in redox pools when growing in physiological conditions (Rahantaniaina *et al.*, 2017). Remarkably, this further indicates that the ASC–GSH cycle is mainly driven by the APX–MDHAR duo rather than by the APX–DHAR–GR trio during fruit development. Then, once established, the redox state was maintained mainly as reduced and continuously decreased during the cell expansion phase (Fig. 5). The concomitant decline in redox and central metabolism activities suggested a decline of global metabolic activity at the expense of osmolyte influx (Beauvoit *et al.*, 2014; Biais *et al.*, 2014). Altogether, cell expansion can be characterised by a rapid transition of ASC to the reduced state and a dynamic maintenance of reduced redox buffers that will gradually decrease, similar to central metabolism.

ROS production and reducing power availability control ASC redox state during the onset of ripening

Finally, ripening is defined physiologically by a reprogramming of metabolism orchestrated by phytohormones, especially ethylene which requires ASC for its synthesis (Dong *et al.*, 1992). Moreover, during ripening, starch is remobilised together with a respiratory burst ending in sugar accumulation and CO_2 release (Colombié *et al.*, 2015; Roch *et al.*, 2020). Interestingly, a stoichiometric model identified that an energy peak appeared just before ripening (Colombié *et al.*, 2017). This is consistent with our data and the similar control pattern of the ASC–GSH cycle observed for 35 DPA and turning models (Table 1), concomitantly with a high sensitivity of ASC redox state and content to NAD(P)H concentration (Fig. S19). In addition, based on enzyme abundance, a prominent part of NAD(P)-dependent features was associated with redox and mitochondrial metabolisms during ripening, as well as active recycling and *de novo* synthesis of NAD(P) (Decros *et al.*, 2019b). Hence, this suggests that carbon resource remobilisation impacts NAD(P) metabolism, which in turn induces the reprogramming of core redox metabolism. Furthermore, CAT capacity increased at turning, while APX capacity remained low concomitantly with an increase in total antioxidant capacity (Fig. 5). However, sensitivity analysis revealed that ROS production strongly influences ASC content and redox state (Fig. S19). Besides, given the accumulation of carotenoids and other secondary metabolites during ripening (e.g. lycopene; Su *et al.*, 2015; Martí *et al.*, 2018), it is likely that

they are also involved in the management of redox metabolism during this phase of development. Therefore, both ROS and reducing power availability appear as major controlling factors of ASC redox state and associated signalling during the onset of ripening, which reinforces the importance of finely tuned ROS production and processing during fruit development.

Oxidised ASC is required for early fruit development

On the other hand, the analysis of ASC-enriched fruits validated the kinetic model and highlighted that ASC fruit content was mainly regulated by its own synthesis (Fig. 3a) and not by import from leaves such as for photoassimilates (Gautier *et al.*, 2009) despite a light-dependent regulation mechanism (Bournonville *et al.*, 2023). Nonetheless, the kinetic model showed an exponential accumulation of reduced ASC above a certain threshold, especially for young fruits. However, young fruit development seems to require an almost total ASC oxidation which is incompatible with a strong ASC synthesis. Indeed, the 8 DPA stage showed a threshold effect for the ASC increase from which signalling through its redox state was hindered, congruent with the developmental disorders observed in homozygous fruits and previous breeding reports (Bulley & Laing, 2016; Deslous *et al.*, 2021).

Acknowledgements

Competing interests

None declared.

Author contributions

PP designed the work with inputs from GD, BB, PB and YG. GD, AF, BB, C Cassan, C Cabasson, TD, KM, MD-N, AD and JJ performed the experiments. GD, BB, PP, SP, SC and PB analysed the data with substantial data interpretation from all the authors. GD and PP wrote the manuscript with inputs from all the authors.

ORCID

Pierre Baldet https://orcid.org/0000-0001-7351-1803
Bertrand Beauvoit https://orcid.org/0000-0002-7666-6429
Cécile Cabasson https://orcid.org/0000-0002-9726-4891
Cédric Cassan https://orcid.org/0000-0003-3022-4278
Sophie Colombié https://orcid.org/0000-0002-9810-4339
Guillaume Decros https://orcid.org/0009-0006-1748-9473
Martine Dieuaide-Noubhani https://orcid.org/0000-0002-9842-9969
Thomas Dussarrat https://orcid.org/0000-0001-6245-3652
Yves Gibon https://orcid.org/0000-0001-8161-1089
Kentaro Mori https://orcid.org/0000-0002-9417-1753
Pierre Pétriacq https://orcid.org/0000-0001-8151-7420
Sylvain Prigent https://orcid.org/0000-0001-5146-0347

Data availability

Metabolic data are provided as supplementary datasets (Dataset S1).

References

Asada K. 1984. Chloroplasts: formation of active oxygen and its scavenging. In: Kyle DJ, Osmond CB, Arntzen CJ, eds. *Methods in enzymology.* Amsterdam, the Netherlands: Elsevier, 422–429.

Baker SM, Schallau K, Junker BH. 2010. Comparison of different algorithms for simultaneous estimation of multiple parameters in kinetic metabolic models. *Journal of Integrative Bioinformatics* 7: 254–262.

Beauvoit BP, Colombié S, Monier A, Andrieu M-H, Biais B, Bénard C, Chéniclet C, Dieuaide-Noubhani M, Nazaret C, Mazat J-P et al. 2014. Model-assisted analysis of sugar metabolism throughout tomato fruit development reveals enzyme and carrier properties in relation to vacuole expansion. *Plant Cell* 26: 3224–3242.

Belouah I, Nazaret C, Pétriacq P, Prigent S, Bénard C, Mengin V, Blein-Nicolas M, Denton AK, Balliau T, Augé S et al. 2019. Modeling protein destiny in developing fruit. *Plant Physiology* 180: 1709–1724.

Bernroitner M, Zamocky M, Furtmüller PG, Peschek GA, Obinger C. 2009. Occurrence, phylogeny, structure, and function of catalases and peroxidases in cyanobacteria. *Journal of Experimental Botany* 60: 423–440.

Biais B, Bénard C, Beauvoit B, Colombié S, Prodhomme D, Ménard G, Bernillon S, Gehl B, Gautier H, Ballias P et al. 2014. Remarkable reproducibility of enzyme activity profiles in tomato fruits grown under contrasting environments provides a roadmap for studies of fruit metabolism. *Plant Physiology* 164: 1204–1221.

Bournonville C, Mori K, Deslous P, Decros G, Blomeier T, Mauxion J-P, Jorly J, Gadin S, Cassan C, Maucourt M et al. 2023. Blue light promotes ascorbate synthesis by deactivating the PAS/LOV photoreceptor that inhibits GDP-L-galactose phosphorylase. *Plant Cell* 35: 2615–2634.

Bowler C, Van Camp W, Van Montagu M, Inzé D, Asada K. 1994. Superoxide dismutase in plants. *Critical Reviews in Plant Sciences* 13: 199–218.

Bulley S, Laing W. 2016. The regulation of ascorbate biosynthesis. *Current Opinion in Plant Biology* 33: 15–22.

Chevalier C, Nafati M, Mathieu-Rivet E, Bourdon M, Frangne N, Cheniclet C, Renaudin J-P, Gévaudant F, Hernould M. 2011. Elucidating the functional role of endoreduplication in tomato fruit development. *Annals of Botany* 107: 1159–1169.

Colombié S, Beauvoit B, Nazaret C, Bénard C, Vercambre G, Le Gall S, Biais B, Cabasson C, Maucourt M, Bernillon S et al. 2017. Respiration climacteric in tomato fruits elucidated by constraint-based modelling. *New Phytologist* 213: 1726–1739.

Colombié S, Nazaret C, Bénard C, Biais B, Mengin V, Solé M, Fouillen L, Dieuaide-Noubhani M, Mazat J-P, Beauvoit B et al. 2015. Modelling central metabolic fluxes by constraint-based optimization reveals metabolic reprogramming of developing *Solanum lycopersicum* (tomato) fruit. *The Plant Journal* 81: 24–39.

Considine MJ, Foyer CH. 2021. Stress effects on the reactive oxygen species-dependent regulation of plant growth and development. *Journal of Experimental Botany* 72: 5795–5806.

New
Phytologist

Cukrov D. 2018. Progress toward understanding the molecular basis of fruit response to hypoxia. *Plants* 7: 78.

Dalton DA, Russell SA, Hanus FJ, Pascoe GA, Evans HJ. 1986. Enzymatic reactions of ascorbate and glutathione that prevent peroxide damage in soybean root nodules. *Proceedings of the National Academy of Sciences, USA* 83: 3811–3815.

Decros G, Baldet P, Beauvoit B, Stevens R, Flandin A, Colombie S, Gibon Y, Pétriacq P. 2019a. Get the balance right: ROS homeostasis and redox signalling in fruit. *Frontiers in Plant Science* 10: 1091.

Decros G, Beauvoit B, Colombié S, Cabasson C, Bernillon S, Arrivault S, Guenther M, Belouah I, Prigent S, Baldet P *et al.* 2019b. Regulation of pyridine nucleotide metabolism during tomato fruit development through transcript and protein profiling. *Frontiers in Plant Science* 10: 1201.

Deslous P, Bournonville C, Decros G, Okabe Y, Mauxion J-P, Jorly J, Gadin S, Brès C, Mori K, Ferrand C *et al.* 2021. Overproduction of ascorbic acid impairs pollen fertility in tomato. *Journal of Experimental Botany* 72: 3091–3107.

Dong JG, Fernández-Maculet JC, Yang SF. 1992. Purification and characterization of 1-aminocyclopropane-1-carboxylate oxidase from apple fruit. *Proceedings of the National Academy of Sciences, USA* 89: 9789–9793.

Fanwoua J, de Visser PHB, Heuvelink E, Yin X, Struik PC, Marcelis LFM. 2013. A dynamic model of tomato fruit growth integrating cell division, cell growth and endoreduplication. *Functional Plant Biology* 40: 1098–1114.

Fernandez-Pozo N, Zheng Y, Snyder SI, Nicolas P, Shinozaki Y, Fei Z, Catala C, Giovannoni JJ, Rose JKC, Mueller LA. 2017. The tomato expression atlas. *Bioinformatics* 33: 2397–2398.

Foyer CH. 2018. Reactive oxygen species, oxidative signaling and the regulation of photosynthesis. *Environmental and Experimental Botany* 154: 134–142.

Foyer CH, Noctor G. 2011. Ascorbate and glutathione: the heart of the redox hub. *Plant Physiology* 155: 2–18.

Foyer CH, Noctor G. 2016. Stress-triggered redox signalling: what's in pROSpect? *Plant, Cell & Environment* 39: 951–964.

Gautier H, Massot C, Stevens R, Sérino S, Génard M. 2009. Regulation of tomato fruit ascorbate content is more highly dependent on fruit irradiance than leaf irradiance. *Annals of Botany* 103: 495–504.

Gibon Y, Blaesing OE, Hannemann J, Carillo P, Höhne M, Hendriks JHM, Palacios N, Cross J, Selbig J, Stitt M. 2004. A robot-based platform to measure multiple enzyme activities in Arabidopsis using a set of cycling assays: comparison of changes of enzyme activities and transcript levels during diurnal cycles and in prolonged darkness. *Plant Cell* 16: 3304–3325.

Hashida S, Miyagi A, Nishiyama M, Yoshida K, Hisabori T, Kawai-Yamada M. 2018. Ferredoxin/thioredoxin system plays an important role in the chloroplastic NADP status of Arabidopsis. *The Plant Journal* 95: 947–960.

Heinrich R, Rapoport TA. 1974. A linear steady-state treatment of enzymatic chains. General properties, control and effector strength. *European Journal of Biochemistry* 42: 89–95.

Hoops S, Sahle S, Gauges R, Lee C, Pahle J, Simus N, Singhal M, Xu L, Mendes P, Kummer U. 2006. COPASI – a complex pathway simulator. *Bioinformatics* 22: 3067–3074.

Jozefczak M, Bohler S, Schat H, Horemans N, Guisez Y, Remans T, Vangronsveld J, Cuypers A. 2015. Both the concentration and redox state of glutathione and ascorbate influence the sensitivity of Arabidopsis to cadmium. *Annals of Botany* 116: 601–612.

Junglee S, Urban L, Sallanon H, Lopez-Lauri F. 2014. Optimized assay for hydrogen peroxide determination in plant tissue using potassium iodide. *American Journal of Analytical Chemistry* 5: 730–736.

Kacser H, Burns JA. 1973. The control of flux. *Symposia of the Society for Experimental Biology* 27: 65–104.

Karpinska B, Zhang K, Rasool B, Pastok D, Morris J, Verrall SR, Hedley PE, Hancock RD, Foyer CH. 2018. The redox state of the apoplast influences the acclimation of photosynthesis and leaf metabolism to changing irradiance: apoplastic redox state regulates light acclimation. *Plant, Cell & Environment* 41: 1083–1097.

Kassambara A, Mundt F. 2020. FACTOEXTRA: extract and visualize the results of multivariate data analyses. *R Package Version* 1.

Kolde R. 2019. PHEATMAP: pretty heatmaps. *R Package Version* 1: 790.

Lê S, Josse J, Husson F. 2008. FACTOMINER: an R package for multivariate analysis. *Journal of Statistical Software* 25: 1–18.

Liu Y, Yang X, Zhu S, Wang Y. 2016. Postharvest application of MeJA and NO reduced chilling injury in cucumber (*Cucumis sativus*) through inhibition of H_2O_2 accumulation. *Postharvest Biology and Technology* 119: 77–83.

Marc F, Brisbarre F, Davin A, Baccaunaud M, Ferrand C. 2004. Évaluation du pouvoir antioxydant (TEAC) d'extraits de végétaux en vue d'utilisations alimentaires. *Sciences des Aliments* 24: 399–414.

Markovic J, Borrás C, Ortega Á, Sastre J, Viña J, Pallardó FV. 2007. Glutathione is recruited into the nucleus in early phases of cell proliferation. *Journal of Biological Chemistry* 282: 20416–20424.

Martí R, Leiva-Brondo M, Lahoz I, Campillo C, Cebolla-Cornejo J, Roselló S. 2018. Polyphenol and L-ascorbic acid content in tomato as influenced by high lycopene genotypes and organic farming at different environments. *Food Chemistry* 239: 148–156.

McAtee P, Karim S, Schaffer R, David K. 2013. A dynamic interplay between phytohormones is required for fruit development, maturation, and ripening. *Frontiers in Plant Science* 4: 79.

de Mendiburu F. 2021. AGRICOLAE: statistical procedures for agricultural research. *R Package Version* 1.

Mhamdi A, Queval G, Chaouch S, Vanderauwera S, Van Breusegem F, Noctor G. 2010. Catalase function in plants: a focus on Arabidopsis mutants as stress-mimic models. *Journal of Experimental Botany* 61: 4197–4220.

Mittler R, Zandalinas SI, Fichman Y, Van Breusegem F. 2022. Reactive oxygen species signalling in plant stress responses. *Nature Reviews Molecular Cell Biology* 23: 663–679.

Mori K, Beauvoit BP, Biais B, Chabane M, Allwood JW, Deborde C, Maucourt M, Goodacre R, Cabasson C, Moing A *et al.* 2019. Central metabolism is tuned to the availability of oxygen in developing melon fruit. *Frontiers in Plant Science* 10: 594.

Ortiz-Espín A, Sánchez-Guerrero A, Sevilla F, Jiménez A. 2017. The role of ascorbate in plant growth and development. In: Hossain MA, Munné-Bosch S, Burritt DJ, Diaz-Vivancos P, Fujita M, Lorence A, eds. *Ascorbic acid in plant growth, development and stress tolerance.* Cham, Switzerland: Springer International Publishing, 25–45.

Pesaresi P, Mizzotti C, Colombo M, Masiero S. 2014. Genetic regulation and structural changes during tomato fruit development and ripening. *Frontiers in Plant Science* 5: 124.

Peskin AV, Winterbourn CC. 2017. Assay of superoxide dismutase activity in a plate assay using WST-1. *Free Radical Biology and Medicine* 103: 188–191.

Pétriacq P, de Bont L, Hager J, Didierlaurent L, Mauve C, Guérard F, Noctor G, Pelletier S, Renou J-P, Tcherkez G *et al.* 2012. Inducible NAD overproduction in Arabidopsis alters metabolic pools and gene expression correlated with increased salicylate content and resistance to Pst-AvrRpm1: inducible NAD overproduction. *The Plant Journal* 70: 650–665.

Pignocchi C, Foyer CH. 2003. Apoplastic ascorbate metabolism and its role in the regulation of cell signalling. *Current Opinion in Plant Biology* 6: 379–389.

Polle A. 2001. Dissecting the superoxide dismutase-ascorbate–glutathione-pathway in chloroplasts by metabolic modeling. Computer simulations as a step towards flux analysis. *Plant Physiology* 126: 445–462.

Pritchard SG, Ju Z, van Santen E, Qiu J, Weaver DB, Prior SA, Rogers HH. 2000. The influence of elevated CO_2 on the activities of antioxidative enzymes in two soybean genotypes. *Functional Plant Biology* 27: 1061.

Queval G, Hager J, Gakiere B, Noctor G. 2008. Why are literature data for H_2O_2 contents so variable? A discussion of potential difficulties in the quantitative assay of leaf extracts. *Journal of Experimental Botany* 59: 135–146.

Queval G, Noctor G. 2007. A plate reader method for the measurement of NAD, NADP, glutathione, and ascorbate in tissue extracts: application to redox profiling during Arabidopsis rosette development. *Analytical Biochemistry* 363: 58–69.

Quinet M, Angosto T, Yuste-Lisbona FJ, Blanchard-Gros R, Bigot S, Martinez J-P, Lutts S. 2019. Tomato fruit development and metabolism. *Frontiers in Plant Science* 10: 1554.

Rahantaniaina M-S, Li S, Chatel-Innocenti G, Tuzet A, Issakidis-Bourguet E, Mhamdi A, Noctor G. 2017. Cytosolic and chloroplastic DHARs cooperate in

oxidative stress-driven activation of the salicylic acid pathway. *Plant Physiology* **174**: 956–971.

Rios-Estepa R, Lange I, Lee JM, Lange BM. 2010. Mathematical modeling-guided evaluation of biochemical, developmental, environmental, and genotypic determinants of essential oil composition and yield in peppermint leaves. *Plant Physiology* **152**: 2105–2119.

Roch L, Prigent S, Klose H, Cakpo C-B, Beauvoit B, Deborde C, Fouillen L, van Delft P, Jacob D, Usadel B *et al.* 2020. Biomass composition explains fruit relative growth rate and discriminates climacteric from non-climacteric species. *Journal of Experimental Botany* **71**: 5823–5836.

Rohwer JM. 2012. Kinetic modelling of plant metabolic pathways. *Journal of Experimental Botany* **63**: 2275–2292.

Salon C, Avice J-C, Colombié S, Dieuaide-Noubhani M, Gallardo K, Jeudy C, Ourry A, Prudent M, Voisin A-S, Rolin D. 2017. Fluxomics links cellular functional analyses to whole-plant phenotyping. *Journal of Experimental Botany* **68**: 2083–2098.

Scalzo J, Politi A, Pellegrini N, Mezzetti B, Battino M. 2005. Plant genotype affects total antioxidant capacity and phenolic contents in fruit. *Nutrition* **21**: 207–213.

Schallau K, Junker BH. 2010. Simulating plant metabolic pathways with enzyme-kinetic models. *Plant Physiology* **152**: 1763–1771.

Sofo A, Scopa A, Nuzzaci M, Vitti A. 2015. Ascorbate peroxidase and catalase activities and their genetic regulation in plants subjected to drought and salinity stresses. *International Journal of Molecular Sciences* **16**: 13561–13578.

Su L, Diretto G, Purgatto E, Danoun S, Zouine M, Li Z, Roustan J-P, Bouzayen M, Giuliano G, Chervin C. 2015. Carotenoid accumulation during tomato fruit ripening is modulated by the auxin-ethylene balance. *BMC Plant Biology* **15**: 114.

Summermatter K, Sticher L, Metraux JP. 1995. Systemic responses in *Arabidopsis thaliana* infected and challenged with *Pseudomonas syringae* pv syringae. *Plant Physiology* **108**: 1379–1385.

Terai Y, Ueno H, Ogawa T, Sawa Y, Miyagi A, Kawai-Yamada M, Ishikawa T, Maruta T. 2020. Dehydroascorbate reductases and glutathione set a threshold for high-light–induced ascorbate accumulation. *Plant Physiology* **183**: 112–122.

Thomas S, Mooney PJF, Burrell MM, Fell DA. 1997. Metabolic control analysis of glycolysis in tuber tissue of potato (*Solanum tuberosum*): explanation for the low control coefficient of phosphofructokinase over respiratory flux. *Biochemical Journal* **322**: 119–127.

Tuzet A, Rahantaniaina M-S, Noctor G. 2019. Analyzing the function of catalase and the ascorbate–glutathione pathway in H_2O_2 processing: insights from an experimentally constrained kinetic model. *Antioxidants & Redox Signaling* **30**: 1238–1268.

Valenzuela J, Manzano S, Palma F, Carvajal F, Garrido D, Jamilena M. 2017. Oxidative stress associated with chilling injury in immature fruit: postharvest technological and biotechnological solutions. *International Journal of Molecular Sciences* **18**: 1467.

Valero E, González-Sánchez MI, Maciá H, García-Carmona F. 2009. Computer simulation of the dynamic behavior of the glutathione–ascorbate redox cycle in chloroplasts. *Plant Physiology* **149**: 1958–1969.

Valero E, Macià H, De la Fuente IM, Hernández J-A, González-Sánchez M-I, García-Carmona F. 2015. Modeling the ascorbate–glutathione cycle in chloroplasts under light/dark conditions. *BMC Systems Biology* **10**: 11.

Vivancos PD, Dong Y, Ziegler K, Markovic J, Pallardó FV, Pellny TK, Verrier PJ, Foyer CH. 2010. Recruitment of glutathione into the nucleus during cell proliferation adjusts whole-cell redox homeostasis in *Arabidopsis thaliana* and lowers the oxidative defence shield: recruitment of GSH into the nucleus. *The Plant Journal* **64**: 825–838.

White CA, Kennedy JF. 1985. Methods of enzymatic analysis, 3rd *edn.* In: Bergmeyer HU, Bergmeyer J, GraRl M, eds. *Metabolites 1: carbohydrates*, vol. VI. Weinheim, Germany: Verlag Chemie.

Xia J, Psychogios N, Young N, Wishart DS. 2009. METABOANALYST: a web server for metabolomic data analysis and interpretation. *Nucleic Acids Research* **37**: W652–W660.

Zechmann B. 2011. Subcellular distribution of ascorbate in plants. *Plant Signaling & Behavior* **6**: 360–363.

Zhang M, Yuan B, Leng P. 2009. The role of ABA in triggering ethylene biosynthesis and ripening of tomato fruit. *Journal of Experimental Botany* **60**: 1579–1588.

Supporting Information

Additional Supporting Information may be found online in the Supporting Information section at the end of the article.

Dataset S1 Metabolic data for redox metabolism during tomato fruit development.

Fig. S1 Bidimensional hierarchical clustering of redox and central metabolite content in wild-type and control lines.

Fig. S2 Hydrogen peroxide content during tomato fruit development and scaled-up. Ascorbate and glutathione content and their associated redox state during tomato fruit development.

Fig. S3 NAD(H) and NADP(H) content and their associated redox state during tomato fruit development.

Fig. S4 Ascorbate peroxidase, catalase, monodehydroascorbate reductase, dehydroascorbate reductase, glutathione reductase and superoxide dismutase capacities (V_{max}) during tomato fruit development.

Fig. S5 Contribution of variables to PC1 and PC2 for principal component analysis shown in Fig. 1(a).

Fig. S6 Principal component analysis of 3742 metabolic features and of 733 putative antioxidant features during tomato fruit development.

Fig. S7 Parameter estimated in the model without (left, orange) or with (right, blue) parietal oxidase.

Fig. S8 Experimental wild-type (green) and predicted content values for ascorbate and H_2O_2.

Fig. S9 Experimental wild-type (green) and predicted content values for glutathione.

Fig. S10 Sum of weighted square errors.

Fig. S11 NADP(H) and its redox state in wild-type and ASC^+ mutant fruits during development.

Fig. S12 NAD(H) and its redox state in wild-type and ASC^+ mutant fruits during development.

Fig. S13 Glutathione reductase, monodehydroascorbate reductase and dehydroascorbate reductase capacities in wild-type and ASC^+ mutant fruits during development.

Fig. S14 Ascorbate peroxidase and catalase capacities in wild-type and ASC^+ mutant fruits during development.

Fig. S15 Effect of an increase in ascorbate (ASC) synthesis (blue) or DHA import (orange) on the pericarp ASC content.

Fig. S16 Experimental mutant (red) and predicted values (blue) for ascorbate, glutathione and H_2O_2.

Fig. S17 Sensitivity coefficient of APX, MDHAR, and CAT fluxes.

Fig. S18 Sensitivity coefficient of APX, MDHAR NAD or NADP-dependent activities.

Fig. S19 Sensitivity coefficient of ascorbate (ASC) total content and ASC oxidation ratio.

Method S1 Untargeted metabolomics data collection and processing.

Table S1 ANOVA P-value for features used in Fig. 1.

Table S2 Biochemical reactions and associated rate equations are included in the model.

Table S3 Parameters setting during tomato fruit development.

Table S4 Michaelis–Menten and rate-constant values used in the model as fixed parameters throughout the development.

Table S5 Ordinary differential equations involved in the model.

Table S6 Experimentally measured total ascorbate (ASC) content in ASC-enriched mutant fruits and corresponding value used for cross-validation.

Please note: Wiley is not responsible for the content or functionality of any Supporting Information supplied by the authors. Any queries (other than missing material) should be directed to the *New Phytologist* Central Office.